ACS Catalysis

Letter

pubs.acs.org/acscatalysis

Synergistic Inhibition of Oxide Formation in Oxidation Catalysis: A First-Principles Kinetic Monte Carlo Study of NO + CO Oxidation at Pd(100)

Juan M. Lorenzi,[†] Sebastian Matera,[‡] and Karsten Reuter*[,†]

[†]Chair for Theoretical Chemistry and Catalysis Research Center, Technische Universität München, Lichtenbergstr. 4, 85747 Garching, Germany

[‡]Fachbereich f. Mathematik u. Informatik, Freie Universität Berlin, Otto-von-Simson-Str. 19, D-14195 Berlin, Germany

Supporting Information

ABSTRACT: Oxide formation under oxygen-rich reaction conditions has independently been reported for both CO oxidation and NO oxidation with Pd single-crystal model catalysts. We present a first-principles kinetic Monte Carlo study addressing the simultaneous occurrence of both reactions at Pd(100) exposed to CO- and NO-containing feeds. Even in most oxygen-rich feeds, very small amounts of NO are found to reduce the surface oxygen coverage well below the level required to induce oxide formation. Even though NO and CO compete for the same surface sites and surface oxygen, the ongoing NO oxidation reactions furthermore lead to a partially strong enhancement of the CO oxidation activity. This highlights synergistic effects of multicomponent gas feeds on both surface composition and catalytic activity that cannot be captured, nor extrapolated from prevalent studies focusing on individual reactions.

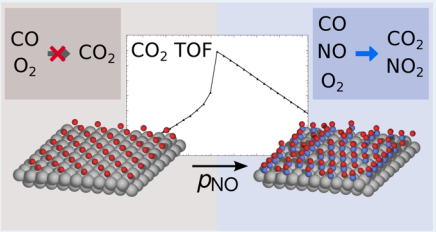

KEYWORDS: *first-principles kinetic Monte Carlo, heterogeneous catalysis, CO oxidation, NO oxidation, oxide formation, NOx reduction, automotive catalysis*

1. INTRODUCTION

The last two decades have seen an extensive (partially heated) discussion, with regard to the active state of late-transition-metal catalysts commonly employed in oxidation catalysis.[1−4] In the oxygen-rich environment, the formation of oxides, thin oxide films, or other heavily oxygen-loaded surface structures would generally be expected for Pt-group metals on thermodynamic grounds. Under operating conditions, this is opposed by the continuing reduction due to the ongoing surface reactions, as well as kinetic limitations to dissociative oxygen adsorption or further oxidation. For the purpose of identifying which effects dominate for the working catalyst, strong efforts have been devoted to identify the surface structure and composition of low-index model catalysts under reaction conditions that come as close as possible to those of technological oxidation catalysis.[5,6] Corresponding near-ambient *in situ* measurements or first-principles microkinetic modeling studies have partially confirmed the formation of oxygen-rich surface structures, partially rejected such formation, or even reported an oscillatory formation and decomposition.[7−13]

While the case is thus not generally settled, an important feature common to previous atomic-scale investigations of single-crystal model catalysts is the consideration of a simplified gas composition, i.e., only the presence of one reducing agent in the feed has been systematically addressed. In the predominantly studied CO oxidation, for instance, this is CO; in NO oxidation, this is NO. This makes the problem more tractable, but neglects possibly important inhibitive or synergistic effects that have frequently been discussed for the multicomponent feeds of real applications.[14−22] Inspired by the automotive exhaust gas composition of lean-burn or diesel engines, we assess this possibility for a gas phase containing both CO and NO and by setting up a first-principles kinetic Monte Carlo model that correspondingly accounts for simultaneous NO and CO oxidation reactions. As the substrate, we specifically select the Pd(100) surface, for which oxide formation has been reported experimentally for both CO oxidation[12] and NO oxidation.[23] The stability, in particular of a monolayer thin PdO(101) surface oxide layer,[24,25] has also been confirmed by constrained *ab initio* thermodynamics and first-principles kinetic Monte Carlo (1p-kMC) studies considering either a CO + O_2[9,11] or a NO + O_2 atmosphere.[26,27] In contrast, a recent 1p-kMC study for CO oxidation at Pd(100) has emphasized the suppression of dissociative O_2 adsorption by higher surface coverages, which kinetically limits the O coverage to values below the threshold inducing oxide formation.[28]

We find that this effect is dramatically increased by the simultaneous presence of NO in the feed. Already smallest amounts of NO, of the order or smaller than, e.g., that typically present under NO_x storage reduction (NSR) conditions,[21,29,30]

Received: May 13, 2016
Revised: July 4, 2016
Published: July 5, 2016

DOI: 10.1021/acscatal.6b01344
ACS Catal. 2016, 6, 5191−5197

are sufficient to reduce the surface oxygen coverage below the values required for oxide formation for a wide range of near-ambient O_2 and CO pressures. Interestingly, this goes hand in hand with a significant increase in the CO oxidation activity for oxygen-rich conditions. Our systematic analysis tracks both effects down to the reduction of kinetic adsorption limitations by additional reaction and diffusion channels offered in the enhanced NO + CO oxidation reaction network. Corresponding synergistic effects in multicomponent gas phases can be neither captured nor extrapolated from studies selectively addressing the catalytic function in feeds containing only subsets of the reactive species.

2. THEORY

We use 1p-kMC simulations[31,32] to numerically evaluate the microkinetics of the NO + CO oxidation reaction network. Different from mean-field rate-equation based microkinetic simulations, 1p-kMC thereby fully treats the correlations, fluctuations, and explicit spatial distributions of the reaction intermediates at the catalyst surface.[33] Targeting steady-state reaction conditions with defined temperature and reactant partial pressures, the 1p-kMC simulations yield the detailed occurrence of any elementary process or local surface configuration within the entire reaction network. Appropriately averaged over a sufficiently large ensemble of surface sites, this leads to the average coverages of all reaction intermediates and to the catalytic activity (measured as turnover frequency (TOF) in product molecules per area and time). As with any microkinetic model, the necessary input to the simulations includes a list of all elementary processes in the reaction network, together with their respective rate constants. The latter are determined using density functional theory (DFT) and transition-state theory (TST).[32,34] To be able to account for the geometric arrangement of the individual surface sites active in the reaction network, 1p-kMC additionally requires this information in the form of a lattice model.

For the CO oxidation part of the reaction network, we rely on the 1p-kMC model established previously by Hoffmann et al.[28,35] Therefore, the following subsections provide first a concise summary of this model and then an account of the computational setup used to obtain the first-principles rate constants and perform the 1p-kMC simulations. This very framework is subsequently employed to extend the CO oxidation model toward (simultaneous) NO oxidation, the details of which are described in subsection 2.3.

2.1. Literature 1p-kMC Model of CO Oxidation at Pd(100). The 1p-kMC model of CO oxidation at Pd(100) by Hoffmann et al.[28,35] considers the high-symmetry hollow and bridge sites as adsorption sites for O and CO, respectively. The list of elementary processes correspondingly contains all nonconcerted adsorption, desorption, diffusion, and Langmuir–Hinshelwood reaction processes involving these sites. Oxygen adsorbs dissociatively and CO unimolecularly. Both processes are nonactivated. The corresponding desorption processes are time reversals of these adsorption processes, with rate constants fulfilling detailed balance. Since CO_2 binds only very weakly to Pd(100), CO oxidation is modeled as associative desorption, i.e., with the formed CO_2 desorbing instantaneously and irreversibly at the temperatures of interest in this study.

Systematic DFT calculations identified strong short-range repulsive interactions between the adsorbed reaction intermediates.[36−38] In the 1p-kMC model, these are accounted for through site-blocking rules that exclude processes leading to O−O pairs at nearest-neighbor (NN) hollow−hollow distances, to CO−CO pairs closer than or at next-NN bridge−bridge distance, and O−CO pairs at NN hollow-bridge distance.[28] Diffusion processes are thus hops between NN sites obeying these site-blocking rules, whereas, for dissociative O_2 adsorption, these rules imply the necessity of a pattern of eight empty hollow sites, such that the two O atoms can adsorb in next-NN sites and have no NNs in any of the surrounding hollow sites (the so-called 8-site rule[28,38]).

2.2. Computational Setup. For the calculation of the first-principles rate constants, we employ the approach described by Reuter and Scheffler.[34] This approach relies on kinetic gas theory to determine the rate constants for adsorption processes, whereas, for bound-to-bound transitions such as surface diffusion or Langmuir–Hinshelwood reactions, harmonic TST is applied. Desorption events are modeled as reverse adsorption processes with rate constants satisfying detailed balance. Gas-phase chemical potentials are interpolated to tabulated values,[28,39,40] which assures correct equilibrium conversion of the gas-phase species. The necessary first-principles input is then essentially reduced to binding energies and reaction barriers. We compute these energetic parameters with DFT and using the plane-wave code CASTEP, together with standard library ultrasoft pseudo-potentials.[41] Electronic exchange and correlation is treated at the level of the generalized gradient approximation functional by Perdew, Burke, and Ernzerhof (PBE)[42] that was also employed in the 1p-kMC model of CO oxidation at Pd(100).[28,35]

The calculations are performed within supercell geometries, using four layer slabs (with the topmost two layers fully relaxed), 3 × 3 surface unit cells, and a 10 Å vacuum. The energetics of the gas-phase molecules is calculated using a 12 Å × 12 Å × 12 Å box and Γ-point sampling. At the employed cutoff of 400 eV and a k-point density of 0.4 $Å^{-1}$ for the supercell calculations, the targeted binding energies and reaction barriers are converged to within 50 meV. Transition-state searches are performed using the climbing-image Nudged Elastic Band (NEB)[43] method. We made sure that all forces at the saddle points were lower than 0.05 eV/Å and also checked the nature of the transition state by calculating the vibrational frequencies using the finite displacement method (keeping the substrate frozen). Both NEB calculations and vibrational analyses are performed within the Atomistic Simulation Environment (ASE).[44]

This computational framework yields energetic parameters that are fully compatible with the literature values of the CO oxidation 1p-kMC model, with small deviations within 70 meV, because of the use of a smaller surface unit cell in the preceding work. A notable exception is presented by the CO oxidation reaction barrier, which was previously estimated by reaction coordinate scans as ∼0.9 eV[28] and is now computed with the NEB method as 0.68 eV (*vide infra*). We confirmed that none of the conclusions presented in ref 28 are affected by this change in the barrier value.

The 1p-kMC model was implemented and run using the kmos computer package.[45] The simulations are performed in simulation cells containing 20 × 20 Pd(100) unit cells (comprising 1200 bridge and hollow sites) and periodic boundary conditions. Test simulations in larger cells containing up to 60 × 60 unit cells showed no evidence of finite size effects. Analogous to the procedure employed by Hoffmann et al.,[28,35] the numerical efficiency of the simulations was increased by raising the barriers of otherwise dominant diffusion

DOI: 10.1021/acscatal.6b01344
ACS Catal. 2016, 6, 5191−5197

processes by 0.5 eV. Validation runs with smaller diffusion barriers showed no significant changes, demonstrating that, even with the raised barriers, diffusion is still fast enough to achieve an equilibration of the adlayer ordering between the other (rare) elementary processes.[32] With these settings, running the simulations over 10^{10} kMC steps was found to be enough to reach steady state and subsequently achieve sufficient sampling for converged average coverages and TOFs.

2.3. Extended 1p-kMC Model of CO + NO Oxidation at Pd(100). The properties of Pd(100) toward NO adsorption and NO reduction to N_2 have been extensively studied both theoretically[46−49] and experimentally.[50−54] Consistent with these works, our DFT calculations at varying coverages indicate a preferential NO adsorption at the high-symmetry bridge sites offered by the Pd(100) surface. These previous studies furthermore suggest that Pd(100) terraces are not very active toward NO dissociation. In particular, both Loffreda et al.[49] and Hammer[48] computed rather high barriers in excess of 1.6 eV for this process. Focusing on oxidizing conditions, we correspondingly neglect NO dissociation events, as well as further reaction channels requiring NO dissociation in the 1p-kMC model and focus on the unimolecular adsorption (and desorption) of NO at bridge sites. This choice is supported *a posteriori* by test simulations that augment our 1p-kMC model with NO dissociation and N_2 formation processes with barriers from ref 48 and that indeed resulted in almost no NO dissociation events occurring in the entire relevant range of gas-phase conditions.

In contrast, NO oxidation yields NO_2 as another reaction intermediate to consider. Different from CO_2, we find NO_2 to bind with moderate strength to Pd(100), requiring its explicit incorporation into the 1p-kMC model. A systematic calculation of NO_2 binding to all Pd(100) high-symmetry sites in upright and tilted configurations (see the Supporting Information (SI)) identifies the tilted on-top configuration shown in Figure 1 as most stable one, with a binding energy of −1.55 eV.

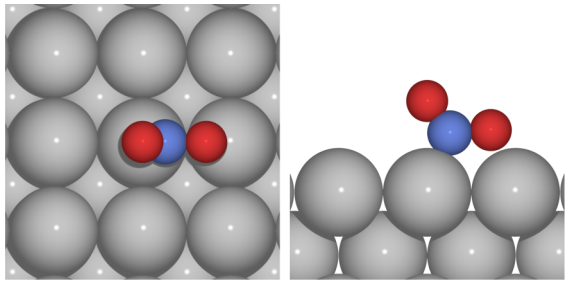

Figure 1. Top view (left) and side view (right) of the optimized adsorption geometry of NO_2 at Pd(100). O, N, and Pd atoms are depicted as red, blue, and gray spheres, respectively.

Similar to CO and O, we suspect sizable lateral interactions also with and between the additional reaction intermediates (NO and NO_2). We computed a DFT database of 97 (co)adsorption configurations in 2 × 2 and 3 × 2 surface unit cells to extract these lateral interactions through pairwise cluster expansions.[36,38] Aiming at higher coverage configurations, we thereby neglect the tilt of the NO_2 adsorption geometry and assume a C_{4v} symmetry in the interactions. As detailed in the SI and irrespective of the particular interaction figures considered in the cluster expansions, this yields strongly repulsive interactions at short range, as previously found for CO oxidation. Consistent with the procedure employed in the original CO oxidation 1p-kMC model,[28,35] we account for these strong interactions through site-blocking rules, suppressing any processes that would lead to top−top, bridge−bridge, top−hollow, top−bridge, and bridge−hollow species at NN distance. In the case of bridge−bridge interactions (NO−NO, NO−CO), this site blocking also extends to a second NN distance across a top site. Similar to the previous findings for CO and O,[28,35] the cluster expansions, in fact, also predict finite-size repulsive interactions at even larger distances. We correspondingly expect the employed shortest-range site-blocking rules to yield a lower bound to the effect of the true interactions. Preliminary 1p-kMC simulations with further ranging site-blocking blocking rules indeed show all the effects discussed below.

Under consideration of the site-blocking rules, all adsorption, desorption, diffusion and reaction processes of the extended CO + NO oxidation model are then essentially defined by the energetic quantities compiled in Table 1. The adsorption processes additionally require a sticking coefficient. Systematic potential energy scans vertically lifting NO and NO_2 from their adsorption site provide no evidence for an additional activation barrier to adsorption. We correspondingly model NO and NO_2 adsorption as nonactivated and use sticking coefficients of 0.5 and 1, respectively, which arises in the hole model underlying the Reuter/Scheffler approach[34] from a straightforward equipartitioning of all impinging molecules over the available active sites per surface unit cell. We note that NO oxidation is a reversible process, which is endothermic in the forward direction (cf. Table 1). Notwithstanding, NO_2 dissociation requires an adjacent empty bridge−hollow second NN site pair, which will favor NO oxidation at higher coverages.[27] For the reaction conditions considered in this study, we treat the desorption of the formed NO_2 as being irreversible, i.e., there is no readsorption of NO_2 from the gas phase. At the low NO_2 TOFs, the underlying assumption thereby is that the small amount of formed NO_2 is quickly swept away with the stream in the reactor geometries typically employed in *in situ* studies on single-crystal model catalysts.[55−57] For channel-type reactors as used for supported real catalysts back-reactions might instead become quite important.[30]

Table 1. Summary of All DFT Binding Energies, As Well As Diffusion and Reaction Barriers Used in the Extended 1p-kMC NO + CO Oxidation Model

parameter	value
Binding Energies	
$E_O^{b,hollow}$	−1.17 eV
$E_{CO}^{b,br}$	−2.00 eV
$E_{NO}^{b,br}$	−2.27 eV
$E_{NO_2}^{b,top}$	−1.55 eV
Diffusion Barriers	
ΔE_O^{diff}	0.24 eV
ΔE_{CO}^{diff}	0.12 eV
ΔE_{NO}^{diff}	0.14 eV
$\Delta E_{NO_2}^{diff}$	0.15 eV
Surface Reactions	
$CO + O \rightarrow CO_2$	
ΔE^{forw}	0.68 eV
$NO + O \leftrightarrow NO_2$	
ΔE^{forw}	1.06 eV
ΔE^{back}	0.32 eV

DOI: 10.1021/acscatal.6b01344
ACS Catal. 2016, 6, 5191−5197

3. RESULTS

3.1. Synergism in the CO + NO Oxidation Activity. We start analyzing the effect of additional NO species present in the feed gas by comparing the CO oxidation activity in the absence of gaseous NO with that resulting in the presence of a small amount of NO, corresponding to $p_{NO} = 10^{-4}$ bar. Figure 2 shows the corresponding results as a function of oxygen and

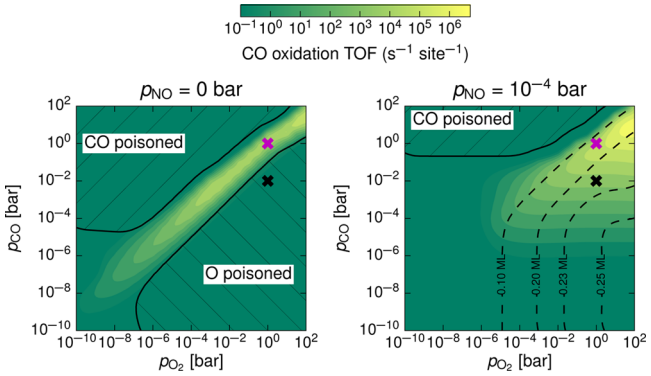

Figure 2. Steady-state CO oxidation turnover frequency (TOF), as a function of oxygen and CO partial pressures at $T = 600$ K, in the absence of additional NO in the feed (left panel) and for a finite amount of NO, corresponding to $p_{NO} = 10^{-4}$ bar (right panel). Hatched lines represent the regions in which the catalyst is poisoned by either CO or oxygen. As the O-poisoned region is absent in the finite p_{NO} case, contour lines for the O coverage are included. The crosses in the diagrams indicate the (p_{O_2}, p_{CO}) conditions used in Figure 3.

CO partial pressures and for a temperature of 600 K. In the absence of NO, we obtain the expected confinement of high catalytic activity to a narrow range of gas-phase conditions around a stoichiometric CO/O_2 partial pressure ratio. Under corresponding pressure ratios (and sufficient absolute pressures), both reaction intermediates, CO and O, are stabilized at the surface in appreciable amounts, which then enables efficient execution of the Langmuir−Hinshelwood-type oxidation reaction. Outside this pressure corridor, the surface gets poisoned by one of the intermediates as also indicated in Figure 2. Under the site-blocking rules employed in the present 1p-kMC model such (O or CO) poisoning corresponds to reaching a maximum coverage of 0.5 monolayer (ML), which then prevents any coadsorption of the respective other species. In the case of O-poisoning, reaching such a critical coverage would, in reality, induce the formation of a surface oxide, which, for Pd(100), is known to start at an O coverage of ≥0.5 ML.[24] For any lower O coverage, we should instead be well inside the applicability regime of the present microkinetic model focusing exclusively on surface reactions at metal Pd(100).[9,11,27,28,35]

Intriguingly, the addition of only a small amount of NO to the feed gas heavily reduces this steady-state O coverage under oxygen-rich conditions. Already for the chosen $p_{NO} = 10^{-4}$ atm, which is at or below the pressures representative for NSR conditions,[21,29,30] no O-poisoning is reached anymore in the entire pressure range displayed in Figure 2. Instead, the oxygen coverage reaches at maximum of ∼0.25 ML, predicting that oxide formation would be clearly inhibited, even under the most oxygen-rich reaction conditions shown. In corresponding environments, the additional NO also leads to a significant increase in the CO oxidation activity, i.e., the active region with appreciable TOFs is much wider in the right panel of Figure 2, while the maximum TOF values reached are barely changed. This positive effect on the CO oxidation properties is quite remarkable considering that CO and NO compete for the same surface sites and for the same adsorbed oxygen species.

3.2. Coverage and Lateral Interactions. In order to analyze these intriguing findings in more detail, we now concentrate on two specific (p_{O_2}, p_{CO}) conditions, which are marked with crosses in Figure 2. Both correspond to a fixed condition of $p_{O_2} = 1$ bar at $T = 600$ K and contrast a situation that, in the absence of NO, is in the high-activity stoichiometric-pressure regime ($p_{CO} = 1$ bar, magenta cross) and a situation that, in the absence of NO, is in the O-poisoned regime ($p_{CO} = 0.01$ bar, black cross). For the sake of simplicity, we will henceforth refer to these two reaction conditions shortly as "high activity" and "poisoned". The top panels of Figure 3 show how the CO and NO oxidation activities change

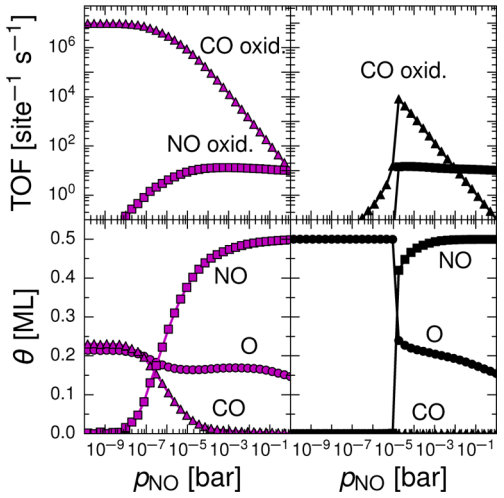

Figure 3. CO and NO oxidation TOFs (top panels) and surface coverages θ (bottom panels), as a function of NO partial pressure and $T = 600$ K. Compared are two specific reaction conditions marked with crosses in Figure 2: $p_{O_2} = 1$ bar, $p_{CO} = 1$ bar (magenta, left panels) and $p_{O_2} = 1$ bar, $p_{CO} = 0.01$ bar (black, right panels), representing high-activity and O-poisoned conditions in the absence of NO, respectively.

for these two cases when the NO pressure is continuously increased. For the "high activity" case, the TOFs evolve smoothly and in a form that is intuitive, in view of the competition of the NO and CO oxidation reactions for the same surface sites and adsorbed oxygen. With increasing p_{NO}, the initially high CO oxidation TOF gradually decreases, at the expense of a continuously rising NO oxidation TOF. In contrast, much more abrupt variations arise in the "poisoned" case. Here, appreciable CO oxidation activity only sets in above a critical p_{NO} (∼10^{-5} atm), then decays again after this initial steep increase. Interestingly, the NO oxidation activity sets in simultaneously with the CO oxidation activity, but then plateaus for higher p_{NO} at exactly the same value as in the "high activity" case.

The key to understanding the less intuitive activity variation of the "poisoned" case comes from an analysis of the surface coverages also compiled in Figure 3 for both cases. For the "high activity" case, we find, at the lowest NO pressures, an O coverage of ∼0.2 ML and a CO coverage at a similar value. This is roughly what thermodynamics wants: If we switch off all oxidation reactions in the 1p-kMC simulations and thereby

DOI: 10.1021/acscatal.6b01344
ACS Catal. 2016, 6, 5191−5197

simulate the adsorption−desorption equilibrium situation, we obtain O and CO coverages of ∼0.3 ML and ∼0.35 ML, respectively, for these pressure conditions. Under the highly repulsive lateral interactions, this is close to the maximum coverage that can be achieved at the surface. The ongoing surface reactions thus remove surface species faster than can be replenished from the gas phase, resulting in average coverages that are below this ideal thermodynamic limit. At increasing p_{NO}, NO starts to compete with CO for the bridge sites. Since NO is subject to the same repulsive lateral interactions with O, this does not affect the O surface population substantially. Its coverage remains almost constant, as is apparent from Figure 3. NO replaces CO at the surface to ultimately reach the maximum possible coverage of 0.5 ML at the highest NO pressures shown. This gradual replacement then effectuates the intuitive smooth TOF variations previously discussed.

The situation is quite different in the "poisoned" case. At the lowest p_{NO}, the ideal thermodynamic coverages resulting from the mere adsorption−desorption equilibrium would be similar to those for the "high activity" case (∼0.3 ML O and ∼0.35 ML CO). In contrast, we see, in Figure 3, the maximum coverage of 0.5 ML O possible in the present 1p-kMC model that concomitantly completely suppresses CO at the surface. This difference from the "high activity" case comes from the changed p_{O_2}/p_{CO} partial pressure ratio. With a ratio of 100:1, CO is now an absolute minority species, which makes replenishment of surface CO through adsorption a much slower process. In consequence, the ongoing surface reactions diminish the surface CO population so much that enough space is created to accommodate more surface oxygen. Under the highly repulsive O−O interactions, this corresponds to a $c(2 \times 2)$ motif. The highly repulsive O−CO interactions then prevent any adsorption of CO into such an oxygen-enriched area. A critical NO pressure is necessary to break this deadlock. Above $p_{NO} \approx 10^{-5}$ atm, NO can be stabilized at the surface, which goes hand in hand with the abrupt reduction of the surface oxygen coverage back to the 0.2 ML case. This frees surface sites for CO adsorption and leads to a strong increase in CO oxidation activity. After this transition, the situation is then equivalent to the "high activity" case with a gradual replacement of CO by NO. Since the NO coverage eventually reaches the same maximum value, the NO oxidation TOF also plateaus at the same value.

3.3. Beyond Coadsorption Effects. From the analysis to this point, it would seem as if the observed positive effect of NO on the "poisoned" case is a simple coadsorption effect, in which the additional presence of NO at the surface helps to suppress the buildup of a poisoning O coverage. Yet, further analysis demonstrates that the cooperativity is more intricate. Selectively switching off the NO oxidation reactions in the 1p-kMC model simulates precisely the effect of a mere coadsorption of (nonreactive) NO. Indeed, such simulations yield a coverage pattern that resembles that discussed for the fully reactive simulations to a large extent, except for a shift in the p_{NO} axis. The "high activity" case exhibits the smooth gradual replacement of CO by NO at bridge sites at ∼0.2 ML O coverage that is essentially independent of p_{NO}. The "poisoned" case shows the abrupt reduction of the O coverage once a threshold NO pressure of $\sim 10^{-4}$ bar is exceeded. Surprisingly, however, these equivalent coverages yield significantly changed CO oxidation TOFs, as summarized in Figure 4. While in the "high activity" case the TOF is

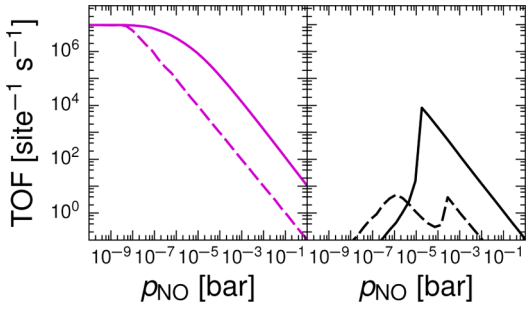

Figure 4. CO oxidation TOFs for the "high activity" (magenta, left panel) and "poisoned" (black, right panel) cases. Compared are the full simulation results as given in Figure 3 (solid lines) to results when the NO oxidation reactions are switched off in the 1p-kMC simulations (dashed lines). Without these reactions, the positive cooperativity is gone and the CO oxidation TOF in the "poisoned" case (black, right panel) remains low at all NO pressures.

systematically lowered by ∼2 orders of magnitude for all but the lowest NO partial pressures, the more striking finding is that, for the "poisoned" case, the CO oxidation TOF remains low for all NO pressures. The "poisoned" case thus remains essentially poisoned, irrespective of an additional presence of NO in the feed. Although we do observe a small enhancing effect due to NO, it is of a much smaller magnitude. In particular, for the intermediate NO pressures just above the threshold at $p_{NO} \approx 10^{-5}$ bar, this implies a quenching of the CO oxidation activity of more than 4 orders of magnitude (cf. Figure 4).

By further modifying the process list considered in the 1p-kMC simulations, we can trace this finding back to the removal of kinetic adsorption limitations by additional reaction and diffusion channels enabled through the NO oxidation part of the reaction network. Both channels bring locally O-poisoned configurations at the surface out of the deadlock situation, by either creating additional NO or CO adsorption possibilities through NO_2 desorption or by diffusional intermixing. Both cases offer increased possibilities to react off adsorbed O and thereby induce the transition from the O-poisoned coverage to a situation with coexisting NO + O already at lower p_{NO}. At these lower p_{NO}, a resulting intermediate NO coverage still leaves sites for CO coadsorption, which, in turn, enables efficient Langmuir−Hinshelwood CO oxidation reactions and the concomitant enhancement of the CO oxidation TOF.

As stated, the effect of the additional reaction channel is thereby simply the creation of free adsorption sites due to the desorption of formed NO_2. We can selectively assess this effect by allowing for the formation and decomposition of surface NO_2 in the 1p-kMC simulations, but disabling the possibility of NO_2 desorption (cf. the SI). More intriguing, however, is the diffusional channel. As illustrated in Figure 5, the formation and subsequent decomposition of a NO_2 reaction intermediate at the surface creates a new O diffusion possibility out of local configurations, where regular hopping diffusion would be suppressed by the repulsive lateral interactions. Because of the endothermicity of the NO oxidation reaction step, the decomposition of a once-formed NO_2 is a likely process, if a neighboring free site and the blocking rules allow for it. We can again selectively assess the effect of this new diffusion channel by restricting NO_2 decomposition only back into the original NO + O configuration out of which the NO_2 was formed in the 1p-kMC simulations. A corresponding suppression of the

DOI: 10.1021/acscatal.6b01344
ACS Catal. 2016, 6, 5191−5197

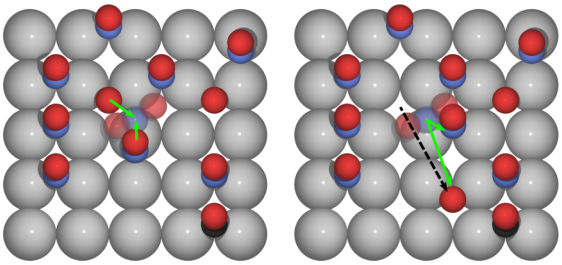

Figure 5. Top view illustrating the additional O diffusion mechanism enabled through the formation (left panel) and subsequent decomposition (right panel) of a NO_2 reaction intermediate. O, N, C, and Pd atoms are depicted as red, blue, black, and gray spheres, respectively.

diffusion mechanism results in TOFs that are only minimally modified from the results shown in Figure 4 when no NO oxidation reactions are allowed to occur at all. Allowing for the diffusion mechanism (i.e., an unrestricted formation and decomposition of NO_2 species) increases the maximum CO oxidation TOF reached already by more than 1 order of magnitude, compared to these no-NO-oxidation results. The remaining difference to the TOFs obtained with the true model with all processes enabled (cf. Figure 4) are then due to the additional reaction channel. While regular coadsorption effects as described in the last section can, to some extent, be extrapolated from separate studies of the individual oxidation reactions, this is neither the case for the additional reaction nor for the diffusion channel. Cooperative effects on the catalytic activity due to such mechanisms are correspondingly missed in traditional studies focusing on idealized feeds containing only one reducing agent.

4. CONCLUSIONS

Fundamental studies that concentrate on establishing microscopic insight into surface catalysis at single-crystal model catalysts largely focus on purified gas feeds containing a minimum number of components. In oxidation catalysis, prominent examples are the reactions of CO oxidation, NO oxidation, or water oxidation, each of which is selectively studied in gas phases containing oxygen plus one reductant (CO, NO, or H_2O, respectively). While this approach reduces the complexity of the problem, it dismisses possible cooperative effects that may arise in multicomponent gas feeds as is common in real applications. We investigated such effects using a 1p-kMC model that describes the simultaneous CO and NO oxidation at a Pd(100) model catalyst. Our results indeed show strong synergistic effects on both the surface composition and the catalytic activity that could not have been extrapolated from the separate study of both oxidation reactions. Very small amounts of NO in the feed gas are sufficient to reduce the surface oxygen coverage well below the level that would otherwise have induced oxide formation in corresponding oxygen-rich environments in CO oxidation catalysis. Simultaneously, this small amount of NO strongly enhances the CO oxidation activity in this oxygen-rich regime, despite competing for the same surface sites and adsorbed oxygen. One key factor behind such nonadditive effects is that already smallest amounts of an additional reaction intermediate (here, NO) may induce surface phase transitions in the adlayer formed by the other intermediates (here, O and CO). This effect is amplified in the presence of strongly repulsive lateral interactions, as is common at late transition-metal surfaces. This complexity cannot be easily captured in prevalent mean-field microkinetic modeling and may thus have been overlooked so far. It can only be grasped with most advanced site-resolved microkinetic analyses, which reveal intricacies in heterogeneous catalysis that continue to surprise us.

■ ASSOCIATED CONTENT

Supporting Information

This material is available free of charge via the Internet at http://pubs.acs.org/. The Supporting Information is available free of charge on the ACS Publications website at DOI: 10.1021/acscatal.6b01344.

NO_2 adsorption configuration search; lateral interaction calculations; analysis of the influence of the blocking-rules scheme; reactivity predicted by the 1p-kMC model with different altered process lists; discussion of the viability of using a mean-field approach (PDF)

■ AUTHOR INFORMATION

Corresponding Author

*E-mail: karsten.reuter@ch.tum.de.

Notes

The authors declare no competing financial interest.

■ ACKNOWLEDGMENTS

We gratefully acknowledge support from the German Research Council (DFG) and the TUM Faculty Graduate Center Chemistry, as well as generous computing time at the Leibniz Rechenzentrum (LRZ) of the Bavarian Academy of Sciences. S.M.'s research is carried out in the framework of MATHEON supported by the Einstein Foundation Berlin. J.M.L. acknowledges enlightening discussions with Max J. Hoffmann.

■ REFERENCES

(1) Reuter, K. In *Nanocatalysis*, 1st Edition; Heiz, U., Landman, U., Eds.; Springer: Berlin, 2006; p 343.

(2) Lundgren, E.; Mikkelsen, A.; Andersen, J.; Kresse, G.; Schmid, M.; Varga, P. *J. Phys.: Condens. Matter* **2006**, *18*, R481−R499.

(3) Over, H. *Chem. Rev.* **2012**, *112*, 3356−3426.

(4) Weaver, J. F. *Chem. Rev.* **2013**, *113*, 4164−4215.

(5) *In-situ Materials Characterization: Across Spatial and Temporal Scales*; Ziegler, A., Graafsma, H., Zhang, X. F., Frenken, J. W. M., Eds.; Springer Series in Materials Science, Vol. *193*; Springer: Berlin, 2014.

(6) Reuter, K. *Catal. Lett.* **2016**, *146*, 541−563.

(7) Gao, F.; Wang, Y.; Goodman, D. W. *J. Phys. Chem. C* **2010**, *114*, 6874−6874.

(8) van Rijn, R.; Balmes, O.; Felici, R.; Gustafson, J.; Wermeille, D.; Westerström, R.; Lundgren, E.; Frenken, J. W. M. *J. Phys. Chem. C* **2010**, *114*, 6875−6876.

(9) Rogal, J.; Reuter, K.; Scheffler, M. *Phys. Rev. Lett.* **2007**, *98*, 046101.

(10) Rogal, J.; Reuter, K.; Scheffler, M. *Phys. Rev. B: Condens. Matter Mater. Phys.* **2007**, *75*, 205433.

(11) Rogal, J.; Reuter, K.; Scheffler, M. *Phys. Rev. B: Condens. Matter Mater. Phys.* **2008**, *77*, 155410.

(12) Hendriksen, B. L. M.; Bobaru, S. C.; Frenken, J. W. M. *Catal. Today* **2005**, *105*, 234−243.

(13) Matera, S.; Blomberg, S.; Hoffmann, M. J.; Zetterberg, J.; Gustafson, J.; Lundgren, E.; Reuter, K. *ACS Catal.* **2015**, *5*, 4514−4518.

(14) Voltz, S. E.; Morgan, C. R.; Liederman, D.; Jacob, S. M. *Ind. Eng. Chem. Prod. Res. Dev.* **1973**, *12*, 294−301.

DOI: 10.1021/acscatal.6b01344
ACS Catal. 2016, 6, 5191−5197

(15) Crocoll, M.; Kureti, S.; Weisweiler, W. *J. Catal.* **2005**, *229*, 480−489.
(16) Irfan, M. F.; Goo, J. H.; Kim, S. D.; Hong, S. C. *Chemosphere* **2007**, *66*, 54−59.
(17) Katare, S. R.; Patterson, J. E.; Laing, P. M. *Ind. Eng. Chem. Res.* **2007**, *46*, 2445−2454.
(18) Koop, J.; Deutschmann, O. *Appl. Catal., B* **2009**, *91*, 47−58.
(19) Pandya, A.; Mmbaga, J.; Hayes, R. E.; Hauptmann, W.; Votsmeier, M. *Top. Catal.* **2009**, *52*, 1929−1933.
(20) Yamashita, H.; Yane, H.; Yamamoto, K. *J. Environ. Eng.* **2011**, *6*, 437−451.
(21) Boubnov, A.; Dahl, S.; Johnson, E.; Molina, A. P.; Simonsen, S. B.; Cano, F. M.; Helveg, S.; Lemus-Yegres, L. J.; Grunwaldt, J.-D. *Appl. Catal., B* **2012**, *126*, 315−325.
(22) Doronkin, D. E.; Kuriganova, A. B.; Leontyev, I. N.; Baier, S.; Lichtenberg, H.; Smirnova, N. V.; Grunwaldt, J.-D. *Catal. Lett.* **2016**, *146*, 452−463.
(23) Weiss, B. M.; Iglesia, E. *J. Catal.* **2010**, *272*, 74−81.
(24) Todorova, M.; Lundgren, E.; Blum, V.; Mikkelsen, A.; Gray, S.; Gustafson, J.; Borg, M.; Rogal, J.; Reuter, K.; Andersen, J. N.; Scheffler, M. *Surf. Sci.* **2003**, *541*, 101−112.
(25) Lundgren, E.; Gustafson, J.; Mikkelsen, A.; Andersen, J.; Stierle, A.; Dosch, H.; Todorova, M.; Rogal, J.; Reuter, K.; Scheffler, M. *Phys. Rev. Lett.* **2004**, *92*, 046101.
(26) Jelic, J.; Meyer, R. J. *Phys. Rev. B: Condens. Matter Mater. Phys.* **2009**, *79*, 125410.
(27) Jelic, J.; Reuter, K.; Meyer, R. *ChemCatChem* **2010**, *2*, 658−660.
(28) Hoffmann, M. J.; Reuter, K. *Top. Catal.* **2014**, *57*, 159−170.
(29) Matsumoto, S. *CATTECH* **2000**, *4*, 102−109.
(30) Koop, J.; Deutschmann, O. Modeling and simulation of NOx abatement with storage/reduction catalysts for lean burn and diesel engines. *SAE Tech. Pap. Ser.* **2007**, Paper No. 2007-01-1142 (DOI: 10.4271/2007-01-1142).
(31) Sabbe, M.; Reyniers, M.-F.; Reuter, K. *Catal. Sci. Technol.* **2012**, *2*, 2010−2024.
(32) Reuter, K. In *Modelling and Simulation of Heterogeneous Catalytic Reactions: From the Molecular Process to the Technical System*; Deutschmann, O., Ed.; Wiley−VCH: Weinheim, Germany, 2013.
(33) Temel, B.; Meskine, H.; Reuter, K.; Scheffler, M.; Metiu, H. *J. Chem. Phys.* **2007**, *126*, 204711.
(34) Reuter, K.; Scheffler, M. *Phys. Rev. B: Condens. Matter Mater. Phys.* **2006**, *73*, 045433.
(35) Hoffmann, M. J.; Scheffler, M.; Reuter, K. *ACS Catal.* **2015**, *5*, 1199−1209.
(36) Zhang, Y.; Blum, V.; Reuter, K. *Phys. Rev. B: Condens. Matter Mater. Phys.* **2007**, *75*, 235406.
(37) Liu, D.-J.; Evans, J. W. *J. Chem. Phys.* **2006**, *125*, 054709.
(38) Liu, D.-J.; Garcia, A.; Wang, J.; Ackerman, D. M.; Wang, C.-J.; Evans, J. W. *Chem. Rev.* **2015**, *115*, 5979−6050.
(39) Chase, M. W.; Curnutt, J. L.; Prophet, H.; McDonald, R. A.; Syverud, A. N. *J. Phys. Chem. Ref. Data* **1975**, *4*, 1−176.
(40) Reuter, K.; Scheffler, M. *Phys. Rev. B: Condens. Matter Mater. Phys.* **2001**, *65*, 035406.
(41) Clark, S. J.; Segall, M. D.; Pickard, C. J.; Hasnip, P. J.; Probert, M. I. J.; Refson, K.; Payne, M. C. *Z. Kristallogr.—Cryst. Mater.* **2005**, *220*, 567−570.
(42) Perdew, J. P.; Burke, K.; Ernzerhof, M. *Phys. Rev. Lett.* **1996**, *77*, 3865−3868.
(43) Henkelman, G.; Uberuaga, B. P.; Jónsson, H. *J. Chem. Phys.* **2000**, *113*, 9901−9904.
(44) Bahn, S.; Jacobsen, K. W. *Comput. Sci. Eng.* **2002**, *4*, 56−66.
(45) Hoffmann, M. J.; Matera, S.; Reuter, K. *Comput. Phys. Commun.* **2014**, *185*, 2138−2150.
(46) Delbecq, F.; Moraweck, B.; Vérité, L. *Surf. Sci.* **1998**, *396*, 156−175.
(47) Delbecq, F.; Sautet, P. *Surf. Sci.* **1999**, *442*, 338−348.
(48) Hammer, B. *J. Catal.* **2001**, *199*, 171−176.
(49) Loffreda, D.; Delbecq, F.; Simon, D.; Sautet, P. *J. Chem. Phys.* **2001**, *115*, 8101−8111.
(50) (a) Nyberg, C.; Uvdal, P. *Surf. Sci.* **1988**, *204*, 517−529; (b) Nyberg, C.; Uvdal, P. *Surf. Sci.* **1991**, *256*, 42−49.
(51) Rainer, D. R.; Vesecky, S. M.; Koranne, M.; Oh, W. S.; Goodman, D. W. *J. Catal.* **1997**, *167*, 234−241.
(52) Yeo, Y. Y.; Vattuone, L.; King, D. A. *J. Chem. Phys.* **1997**, *106*, 1990−1996.
(53) Daté, M.; Okuyama, H.; Takagi, N.; Nishijima, M.; Aruga, T. *Surf. Sci.* **1996**, *350*, 79−90.
(54) Jorgensen, S. W.; Canning, N. D. S.; Madix, R. J. *Surf. Sci.* **1987**, *179*, 322−350.
(55) Matera, S.; Reuter, K. *Catal. Lett.* **2009**, *133*, 156−159.
(56) Matera, S.; Reuter, K. *Phys. Rev. B: Condens. Matter Mater. Phys.* **2010**, *82*, 085446.
(57) Matera, S.; Maestri, M.; Cuoci, A.; Reuter, K. *ACS Catal.* **2014**, *4*, 4081−4092.

DOI: 10.1021/acscatal.6b01344
ACS Catal. 2016, 6, 5191−5197